(Received 10 July 2025, Accepted 20 August 2025, Scheduled 29 August 2025)

A MIMO Ultra-Wideband Antenna with High Isolation and Triple Notches

Rongjiaxu Tu, Han Lin*, and Zhonggen Wang

School of Electrical and Information Engineering, Anhui University of Science and Technology, Huainan 232001, China

ABSTRACT: This paper proposes a four-port ultra-wideband (UWB) MIMO antenna with high isolation and three notch bands. A cross-shaped decoupling structure (CSDS) is synergistically integrated with an improved L-shaped ground plane to achieve high port isolation. Composite resonant slots (CRSs) are introduced on the radiating patch, and two L-shaped slots are etched on the feed line to suppress interferences from WiMAX (3.19 GHz), C-band (4.45 GHz), and X-band (7.95 GHz). Simulation and measurement results verify that the Voltage Standing Wave Ratio (VSWR) at the center frequencies of the notched bands is greater than 6.8, 8.1, and 4.3, respectively. In the operating frequency band of 2.7–12 GHz (excluding the notched bands), the isolation is > 24.3 dB, envelope correlation coefficient (ECC) < 0.0045, diversity gain (DG) > 9.9990 dB, total active reflection coefficient (TARC) < -10 dB, and channel capacity loss (CCL) < 0.4 bps/Hz. It fully meets the requirements of high-performance MIMO systems for channel independence and transmission efficiency. Compared with similar studies, this work has significant advantages in core indicators such as bandwidth, number of notched bands, and isolation, providing new ideas for the design of UWB-MIMO systems in complex electromagnetic environments.

1. INTRODUCTION

Ultra-wideband (UWB) technology, as a short-range wireless communication solution, can achieve stable and high-speed data transmission. It has the advantages of high data rate, high-precision positioning, rapid transmission, and is applicable to biomedical imaging, sensor networks, and other fields [1]. UWB has emerged as an important candidate technology in modern wireless communication systems. Although the traditional UWB technology performs excellently in achieving high data rates and low costs, multipath propagation still brings impacts that are difficult to avoid [2]. Combining UWB wireless communication system with MIMO technology provides an effective way to solve this problem. By utilizing multiple channels to transmit data in parallel, multiple-input multiple-output (MIMO) technology can not only significantly enhance the system capacity but also improve the communication quality through spatial diversity. It is an effective means to mitigate the impact of multipath fading [3].

The Federal Communications Commission (FCC) of the United States has designated the frequency band from 3.1 to 10.6 GHz as the commercial spectrum for UWB technology. However, due to the wide spectrum range of UWB, there are multiple interference frequency bands that overlap with those of other systems. For example, the frequency band of 3.3 to 3.7 GHz is used for WiMAX (IEEE 802.16); the band from 3.8 to 4.2 GHz corresponds to C-band satellite communication; the range of 5.15 to 5.825 GHz is utilized for Wireless Local Area Network (WLAN, such as IEEE 802.11a and HIPERLAN/2); the 7.25 to 7.75 GHz band belongs to X-band satellite communication; and the 8.025 to 8.4 GHz band is the frequency band specified by the International Telecommunication Union (ITU). These frequency bands may cause interference to UWB wireless communication system [4]. Therefore, it is of great significance to mitigate these interferences within the UWB. In some applications, people usually suppress the interference signals in a UWB system by integrating a filter at the front end of the antenna. However, this method will increase the complexity and cost of the system. For this reason, designing a UWB-MIMO antenna with notch characteristics becomes a more effective solution [5–7]. Ref. [8] describes, in detail, a crescent-shaped double-sided MIMO antenna structure composed of four elements. This design effectively improves the isolation performance among antenna ports by introducing the technologies of pattern diversity and polarization diversity. The test results indicate that within the operating bandwidth of 12.4 GHz, the inter-port isolation in most frequency bands exceeds 20 dB. Ref. [9] adopts a CSDS, achieving a high isolation of more than 19 dB. By etching two C-shaped slots on each radiator, a notch antenna suitable for the WLAN and X-band is realized. At the same time, an L-shaped slot is introduced on the ground to achieve the function of a notch antenna for WiMAX. Inspired by this research, the MIMO system in this paper also introduces pattern and polarization diversity strategies, and adopts a cross-shaped decoupling structure (CSDS), which effectively improves the isolation between antennas, thereby reducing the signal interference. It has achieved excellent results in the simulation verification, further confirming the effectiveness of this approach in improving the performance of MIMO antennas. In [10–26], various methods are employed to design notch characteristics, such as introducing parasitic structures, closed-loop resonators, metamaterials, slots, stubs, stub resonators, and loading filter structures, among others. Based on these technologies, researchers have developed UWB-MIMO antennas with notch capabilities for single band, dual bands, and triple bands. Although re-

* Corresponding author: Han Lin (hanlin@aust.edu.cn).

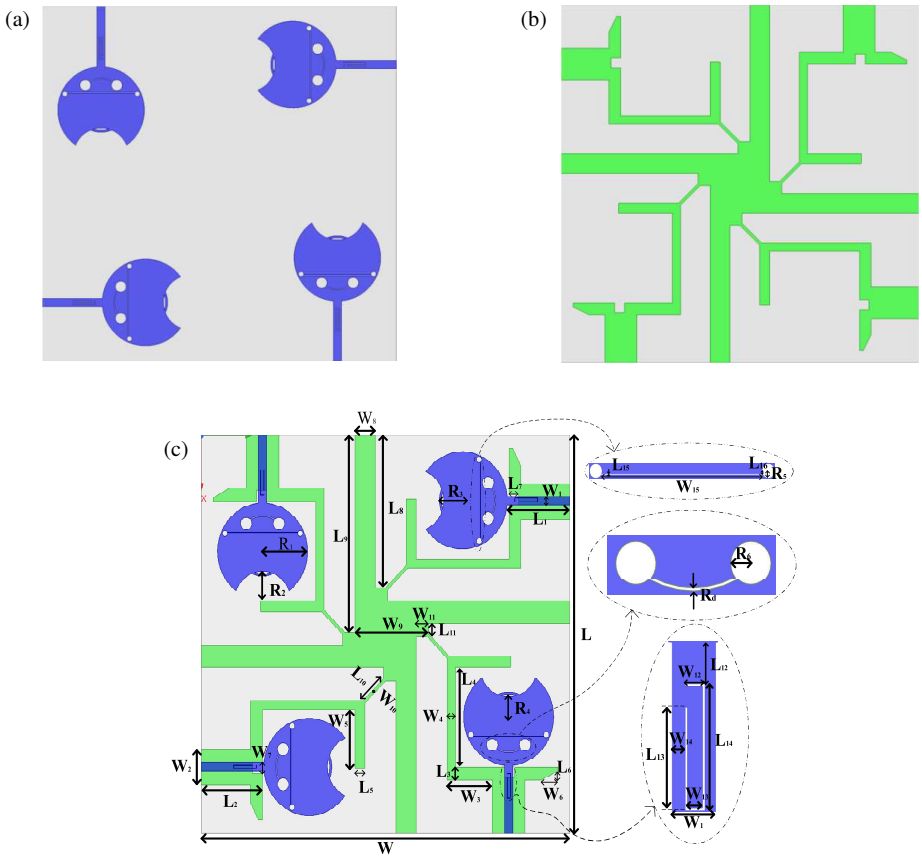

FIGURE 1. Dimensional parameters of proposed antenna. (a) Top-layer structure diagram; (b) Bottom-layer structure diagram; (c) Key dimensional parameters of the antenna structure.

searchers have proposed various methods to achieve the band-notch characteristics of antennas in recent years, these methods are generally traditional. The notch structures are mostly designed on radiating patches or ground planes, and it is rare to introduce notch structures in feeder parts. To address this challenge, we propose a high-isolation UWB-MIMO notch antenna. The designed antenna exhibits an isolation performance exceeding 24.3 dB, significantly enhancing system performance. Within its UWB operating bandwidth, we introduce two distinct types of composite resonant slots (CRSs) etched on the radiating patch and an L-shaped slot on the feeder, and the antenna generates notches that effectively suppress three separate frequency bands.

2. ANTENNA DESIGN PROCESS

2.1. Antenna Geometry

The design of the proposed antenna is composed of four orthogonally arranged improved circular metal radiating patches, combined with an optimally designed L-shaped stub floor structure. Meanwhile, a CSDS is introduced to enhance port isolation. This antenna is designed and implemented based on an FR4 dielectric substrate with a relatively low cost, a relative permittivity of 4.4, and a loss tangent of 0.02. The overall size of the antenna is $90 \times 90 \times 1.2\,\text{mm}^3$. Figs. 1(a)–(c) respectively show the top view, bottom view of the antenna, and its detailed

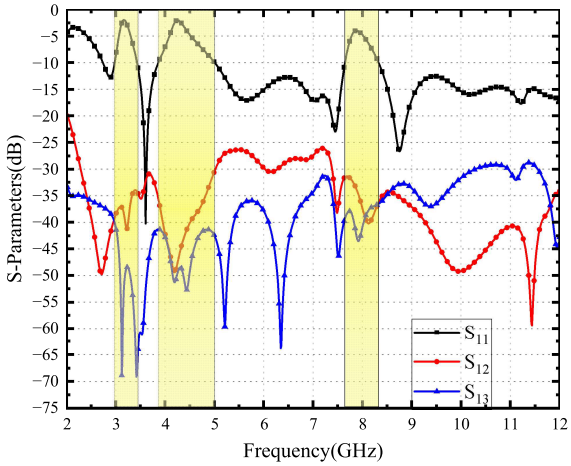

FIGURE 2. Simulated S-parameters of proposed triple notched MIMO antenna characteristics.

dimensional parameters, including the specific structural parameters of the etched slots. The final optimized dimensions of the antenna are shown in Table 1. Fig. 2 presents the simulated S-parameter results of this antenna. The simulation indicates that the antenna exhibits good impedance matching performance within the frequency band of 2.87–12 GHz and achieves effective notch characteristics in three frequency bands, namely 2.95–3.41 GHz, 3.84–4.98 GHz, and 7.63–8.31 GHz. Throughout the entire operating frequency band, the isolation between

TABLE 1. Optimized dimension of antenna parameters.

Parameter	L	L_1	L_2	L_3	L_4	L_5	L_6	L_7	L_8
Size (mm)	90	15.3	15	3	22.5	2.5	1	2.5	34.5
Parameter	L_9	L_{10}	L_{11}	L_{12}	L_{13}	L_{14}	L_{15}	L_{16}	W
Size (mm)	44.5	7.07	2.5	1.82	4.9	5.6	0.1	0.25	90
Parameter	W_1	W_2	W_3	W_4	W_5	W_6	W_7	W_8	W_9
Size (mm)	2	8	11	2	13.5	4	2.5	5	18
Parameter	W_{10}	W_{11}	W_{12}	W_{13}	W_{14}	W_{15}	R_1	R_2	R_3
Size (mm)	0.5	3	0.9	0.7	0.6	17.2	11	7	6.4
Parameter	R_4	R_5	R_6	R_d					
Size (mm)	6.8	0.64	1.6	0.5					

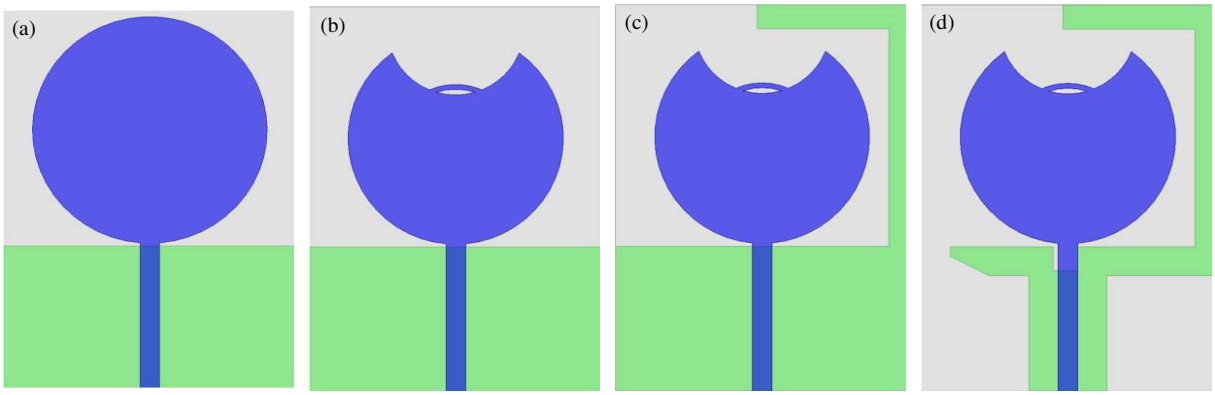

FIGURE 3. Proposed single antenna evolution steps; (a) Antenna 1; (b) Antenna 2; (c) Antenna 3; (d) Antenna 4.

the antenna ports exceeds 24.3 dB, showcasing outstanding decoupling performance.

2.2. Proposed Single Antenna Evolution

Figure 3 shows the evolution process of the proposed monopole antenna, and Fig. 4 presents the changes in S_{11} parameters of the antenna during all the evolution stages. The initially designed antenna named Antenna 1 consists of a simple circular patch radiator with a radius of 11 mm and a partial ground plane. It operates in the frequency bands of 2.7 GHz to 4.2 GHz and 9.9 GHz to 11.2 GHz, but the reflection coefficient of this design fails to cover the entire UWB range. To improve impedance matching and expand the operating frequency, the original circular shape was cut, and an arc was added. This modification is equivalent to adding a capacitor, enhancing the antenna's impedance matching capability. Thus, Antenna 2 was formed. To further optimize the performance, an L-shaped stub was introduced on the ground plane, thereby generating Antenna 3. Due to the addition of the stub, the radiation pattern of the antenna changed as shown in Fig. 5. Building on this change, the ground plane structure was further modified to yield Antenna 4. Eventually, the antenna's operating frequency band was extended to 2.87 GHz to 12 GHz, meeting the application requirements of UWB and partial X-band. As observed from Fig. 5, without the inclusion of the L-shaped stub, the radiation pattern is symmetrically distributed along both sides of the feeder direction, with part of the radiation concentrated near the outer edge of the antenna. This would lead to increased coupling between antennas in multi-input scenarios, affecting the isolation performance. After the L-shaped stub is added, the radiation near the antenna edges is reduced. This modification not only causes the radiation to contract inward more, enhancing the directivity of the antenna, but also helps reduce mu-

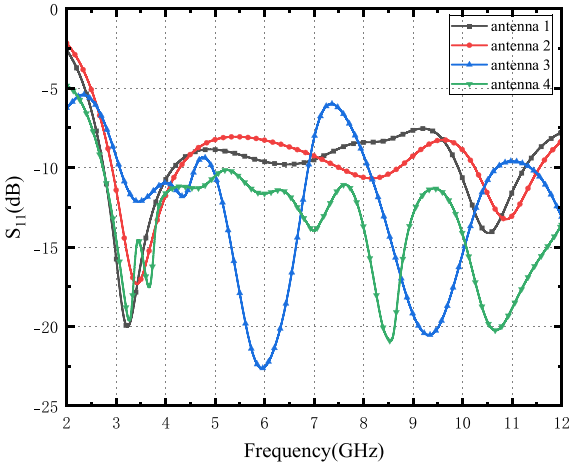

FIGURE 4. Simulated S_{11}-parameters of Antennas 1–4.

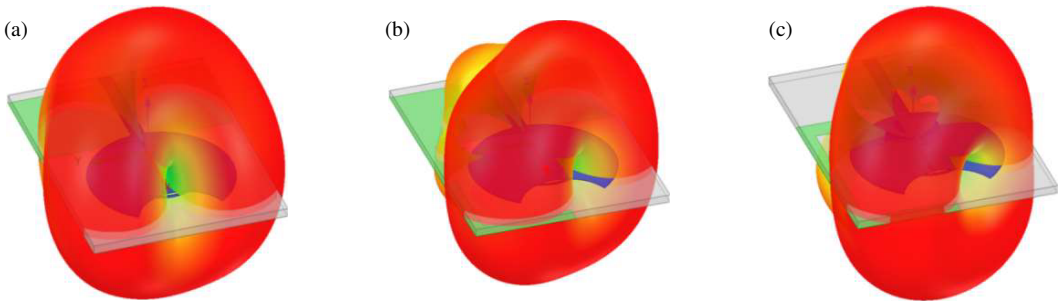

FIGURE 5. Single antenna 3-D radiation pattern; (a) Antenna 2; (b) Antenna 3; (c) Antenna 4.

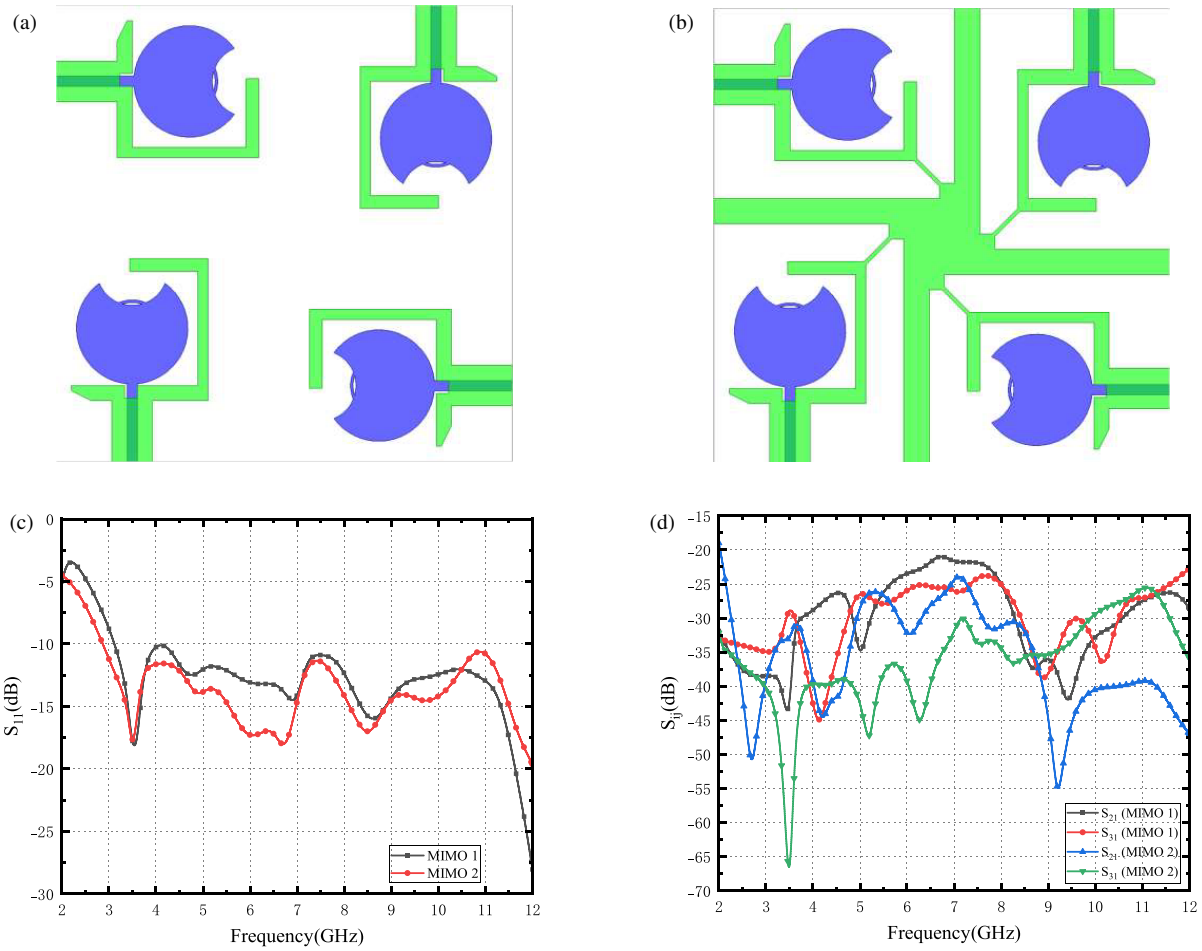

FIGURE 6. Influence of the CSDS on the antenna's S-parameters; (a) Without CSDS; (b) With CSDS; (c) S_{11} parameter of the antenna; (d) Isolation parameter of the antenna.

tual coupling between antennas in future MIMO applications, thereby improving the overall system performance.

2.3. Proposed Four-Port MIMO Antenna Evolution

To further enhance the antenna's performance in terms of reliability, signal quality, and data transmission rate, this section will discuss the evolution process of a four-port MIMO antenna, as shown in Figs. 6(a) and 6(b). Arranging Antenna 4 in an orthogonal manner formed the initial four-port antenna named MIMO 1, achieving a bandwidth of 3.12 GHz to 12 GHz with an isolation degree exceeding 20.9 dB between ports.

To further improve the isolation, a CSDS was introduced and connected to the ground plane based on MIMO 1, forming MIMO 2. This modification improved the isolation to over 24.3 dB. As distinctly illustrated in Fig. 6(c), the variations in S_{11} parameters of MIMO 1 and MIMO 2 are evident when comparing the scenarios before and after the introduction of the CSDS structure. Fig. 6(d) shows the S-parameters S_{12} and S_{13} of MIMO 1 and MIMO 2, corresponding to the isolation between adjacent ports and diagonal ports, respectively. After the CSDS was added, a slight increase in isolation between adjacent ports was observed, while the isolation between diagonal

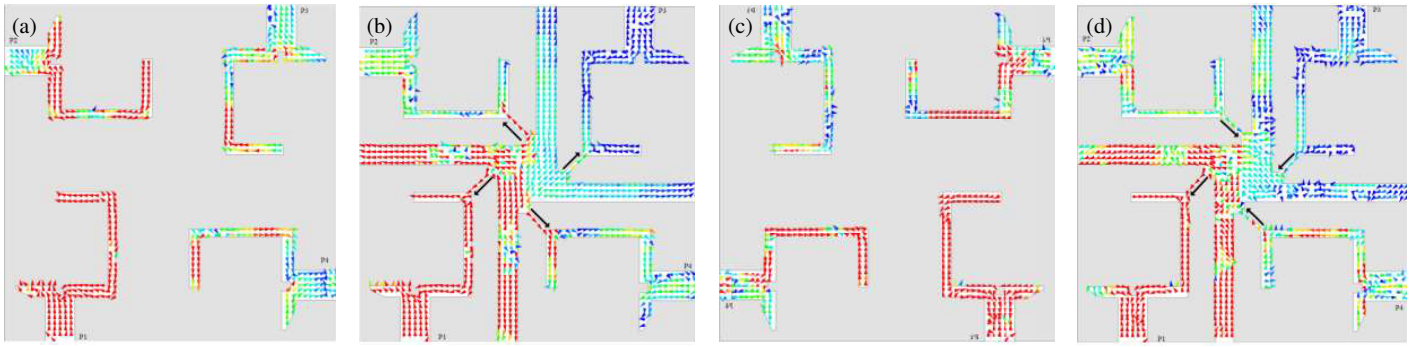

FIGURE 7. Vector current diagrams on the back of the antenna; (a) 3.7 GHz without CSDS; (b) 3.7 GHz with CSDS; (c) 5.6 GHz without CSDS; (d) 5.6 GHz with CSDS.

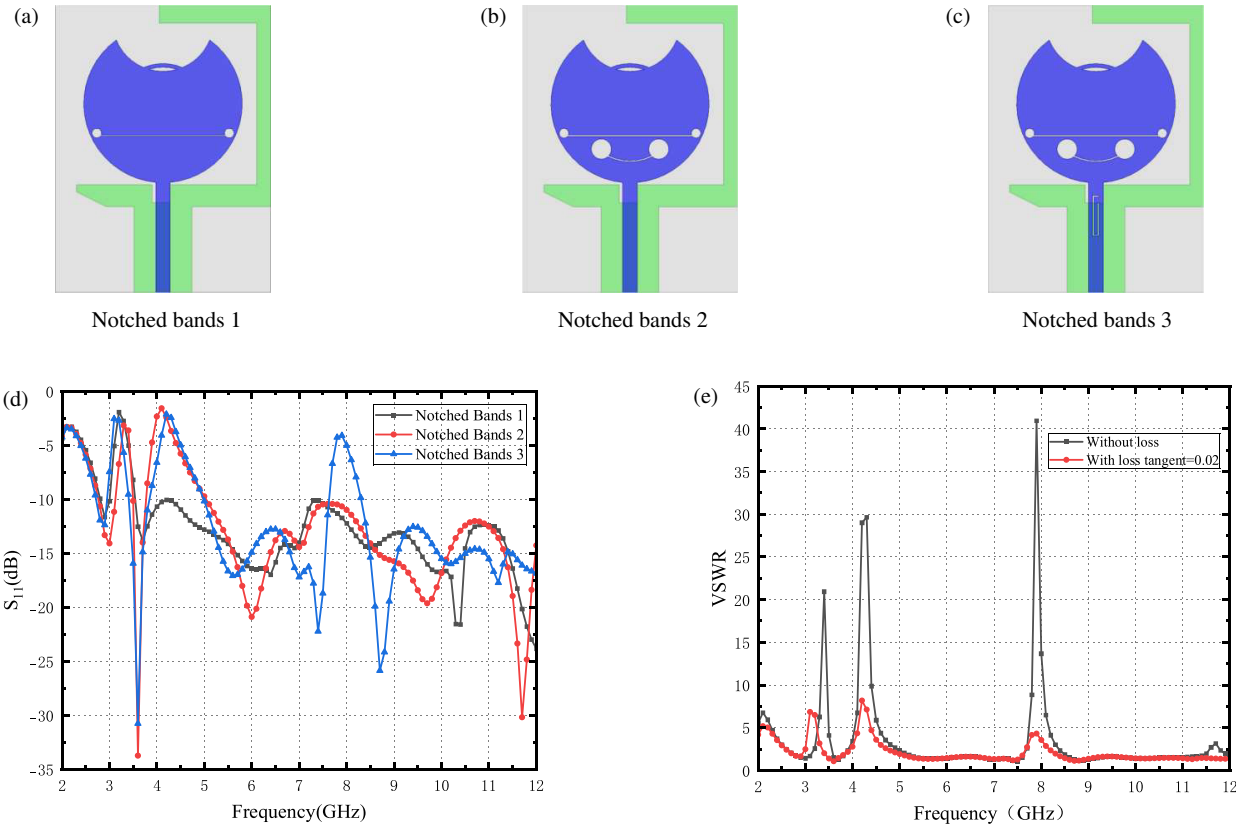

FIGURE 8. (a) Notched bands 1; (b) Notched bands 2; (c) Notched bands 3; (d) S_{11} parameters; (e) VSWR.

ports was significantly enhanced in the 3.7 GHz and approximately 5.6 GHz frequency bands.

Fig. 7 compares the vector current distribution diagrams at the frequency points of 3.7 GHz and 5.6 GHz with and without CSDS. As clearly shown in the figure, when CSDS is not used, strong induced currents are generated on other ground planes; after adopting this decoupling structure, these induced currents are significantly reduced. This is because the CSDS introduces new coupling paths. Near 3.5 GHz, vector currents flow to each ground plane through the cross-shaped structure, partially canceling the original coupling effect. At 5.6 GHz, currents flow from each ground plane into the cross-shaped structure via connection lines, achieving a current-shunting effect. Overall, this design reduces current coupling and enhances the isolation between ports, thereby effectively improving the performance of the entire MIMO system.

2.4. Notch Structure Design

To effectively suppress narrowband interference within the UWB frequency band, this subsection designs a multi-frequency notch structure. By introducing two different types of CRS on the radiation patch and an L-shaped slot on the feeder line, the control over three-band notch characteristics is achieved. The specific design steps are shown in Figs. 8(a)–(c), and the S_{11} parameters during the evolution process are shown

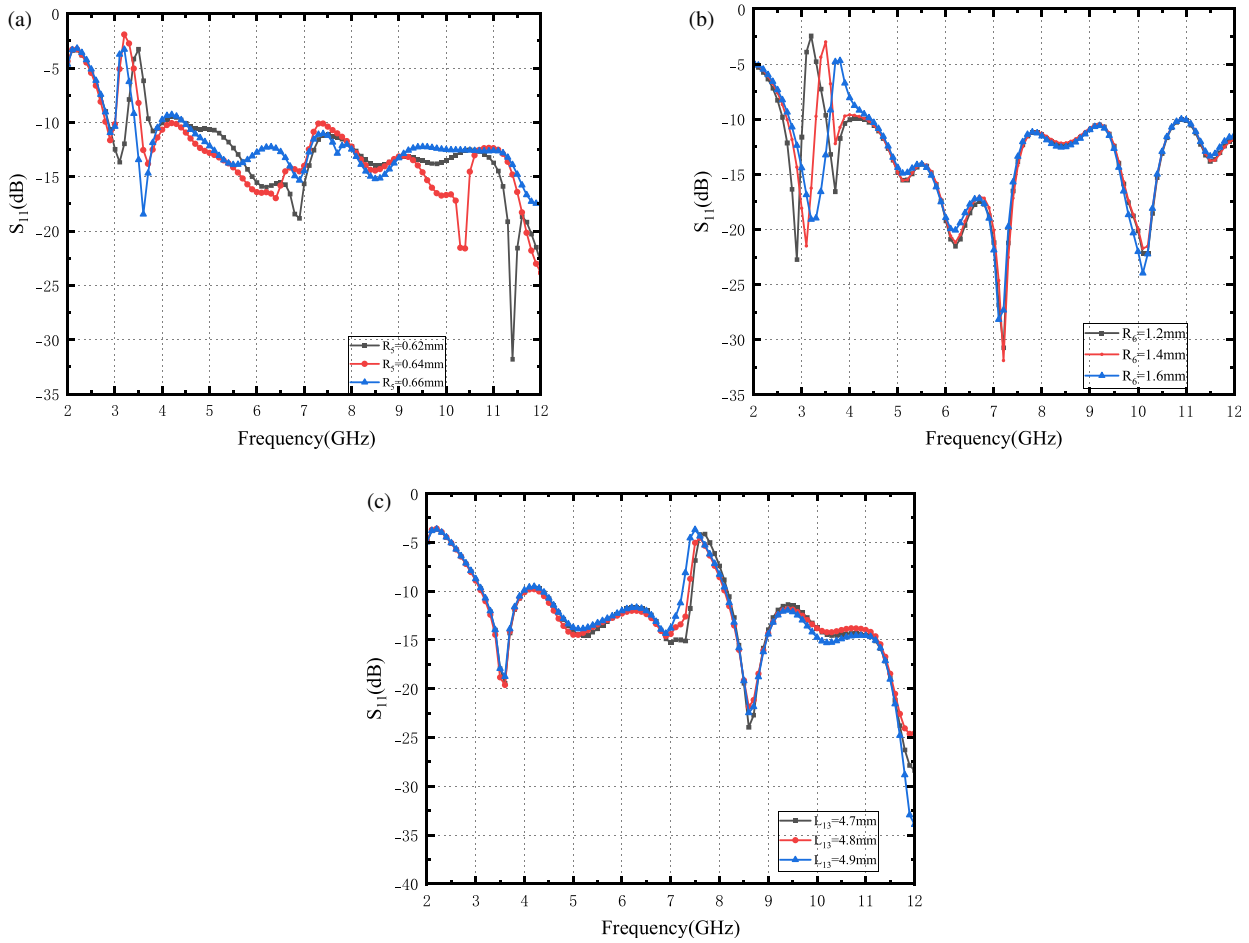

FIGURE 9. S-parameters for dimension variations; (a) R_5; (b) R_6; (c) L_{13}.

in Fig. 8(d). First, two circular regions with a radius of R_5 and one rectangular region with a length of W_{15} and width of L_{15} are removed from each radiation patch. This configuration creates the first notch at the 2.95–3.41 GHz band (centered at 3.19 GHz). Next, two circular regions with a radius of R_6 and an arc-shaped structure with a width of R_d are further removed from each patch, creating a second notch in the 3.84–4.98 GHz band (centered at 4.45 GHz). Finally, two L-shaped slots are introduced in the feeder line to excite a third notched frequency band, ranging from 7.63 GHz to 8.31 GHz (with a center frequency of 7.95 GHz). The introduction of slots in the feeder line distorts the local current distribution of the antenna, leading to fluctuations in other notched frequency bands. Nevertheless, these fluctuations remain within an acceptable range overall.

Among them, the dimensions of L-shaped slots can be accurately calculated through relevant formulas to achieve the required frequency suppression characteristics.

$$L_{\text{slot}} = \frac{c}{2f_{\text{notch}}\sqrt{(\varepsilon_r+1)/2}} \tag{1}$$

where L_{slot} is the total length of the L-shaped slot, and its unit is millimeters; c is the speed of light in vacuum, and its unit is m/s; f_{notch} is the center frequency of the notch, and its unit is Hz; ε_r is the dielectric constant of the substrate (1).

Voltage standing wave ratio (VSWR) is a critical indicator reflecting the impedance matching degree in radio frequency (RF) circuits. In the lossless case: The VSWR values near 3.2 GHz, 4.2 GHz, and 7.9 GHz are 20.9, 29.6, and 40.9, respectively. When the loss tangent is 0.02, Fig. 8(e) shows that the corresponding VSWR values near these frequencies decrease to 6.8, 8.1, and 4.3, respectively. The notch antenna achieves suppression of specific frequency signals by generating high VSWR at the designed notch center frequencies. In the lossless scenario, the notch function is well realized. However, in practical applications, the presence of losses degrades the notch effect to some extent, though it still suppresses the corresponding frequency signals to a certain degree.

Figure 9 investigates the influence of different geometric parameters of the proposed antenna on the notch characteristics. Parameter optimization for each notched element is performed individually by changing only one parameter while keeping all other design factors constant. From the comparison of the three curves, it can be observed that as R_5 increases, the corresponding notch band shifts from a relatively higher frequency to a lower frequency, while the bandwidth of the notch remains unchanged. Similarly, by changing the size of R_6, the notch range

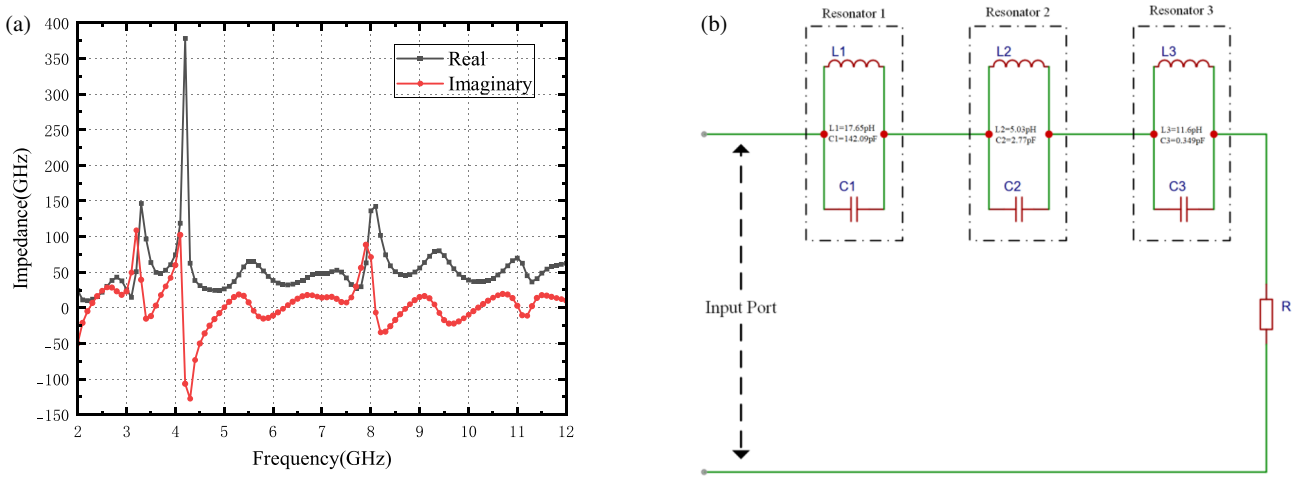

FIGURE 10. (a) Antenna impedance; (b) Equivalent circuit diagram of the 3-notch UWB antenna.

shifts from lower frequencies to higher frequencies. Additionally, as L_{13} is adjusted, the range of the notch band remains unchanged, but the center frequency of the notch decreases. From this, it can be concluded that using the designed method, the notch band can be easily realized and controlled to meet practical requirements simply by adjusting the dimensions of the notch elements. It is also worth noting that changing the parameters of the notch elements only affects the notch band, while the return loss in the remaining UWB frequency bands remains essentially unchanged.

3. ANTENNA PERFORMANCE ANALYSIS

3.1. Equivalent Circuit Analysis

Figure 10(a) illustrates the real and imaginary components of the antenna impedance. As depicted, near 3.2 GHz, 4.2 GHz, and 7.9 GHz, the real components of the input impedance exhibit sharp peaks, signifying abnormally high impedance values. This anomaly induces antenna impedance mismatch, drastically reducing the current fed into the feeder at these three frequencies. Consequently, the antenna fails to radiate efficiently, instead forming band-stop characteristics that produce the notching effect. Fig. 10(b) illustrates the equivalent circuit of the proposed antenna, where the notch structures are respectively modeled as three LC parallel resonant circuits in the circuit. The approximate values of inductance L and capacitance C can be calculated using the following formulas:

$$Q_i = \frac{f_i}{\mathrm{BW}_i} \tag{2}$$

$$C_i = \frac{Q_i}{2\pi f_i R_i} \tag{3}$$

$$L_i = \frac{C_i}{(2\pi f_i)^2} \tag{4}$$

where Q is the quality factor, i the resonator serial number, f the center frequency of the notch, and BW the bandwidth of the notch band. The specific data are shown in Table 2.

TABLE 2. Parameters of the RLC resonant circuit.

f_i (GHz)	BW_i (GHz)	Q_i	R_i (Ω)	C_i (pF)	L_i (pH)
3.2	0.46	6.91	50.99	142.09	17.65
4.2	1.14	3.87	378.03	2.77	5.03
7.9	0.68	11.62	62.9	0.349	11.6

3.2. Antenna Current Analysis

The current distribution across the antenna surface provides an intuitive representation of the operational state of each structural component at specific frequencies. By examining the density or sparsity of current flow, the impact of structural geometries on current transmission paths can be analyzed. Fig. 11 illustrates the current vector distribution at Port 1 under excitation at different notch center frequencies. The current orientations on the patch corroborate the design rationale of achieving notching characteristics through the introduction of slots. At 3.4 GHz, the current primarily concentrates near the slots connecting the two circular and rectangular structures. The vector currents flow in opposite directions along both sides of the slots, creating mutually repulsive current fields in this region. This phenomenon suppresses effective radiation, forming a distinct notching characteristic near this frequency. At 4.2 GHz, the current concentrates around the slots formed by circular and arc-shaped structures. Vector currents flow from the midpoint of the arc toward both sides and are repelled by the currents on the two sides, preventing significant radiation from being generated. When being excited at 7.9 GHz, the current primarily concentrates near the two L-shaped slots on the feeder. As indicated by the vector current distribution, after flowing into the feeder, most of the current propagates along both sides of the L-shaped slots and eventually converges at the gap between the two slots, forming a local circulating current. This traps the current within the area enclosed by the L-shaped structure, resulting in almost no effective radiation near 7.9 GHz.

Figure 12 further demonstrates a comparative visualization of current distributions at the frequency points of 3.4 GHz, 4.2 GHz, and 7.9 GHz. It is evident that the current con-

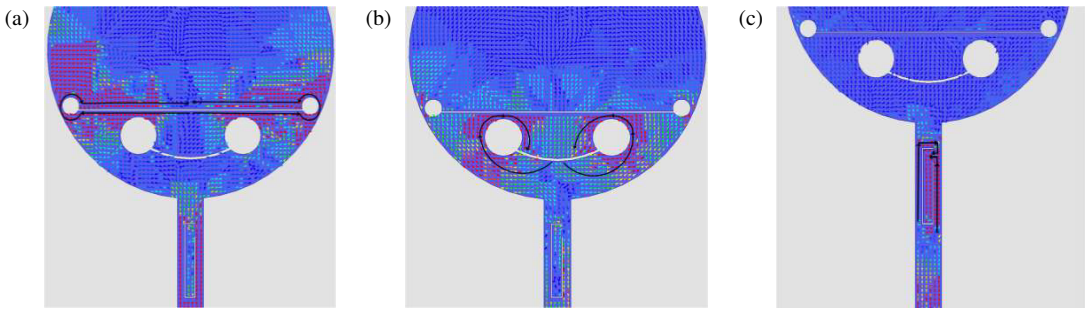

FIGURE 11. Vector current diagram (a) 3.4 GHz; (b) 4.2 GHz; (c) 7.9 GHz.

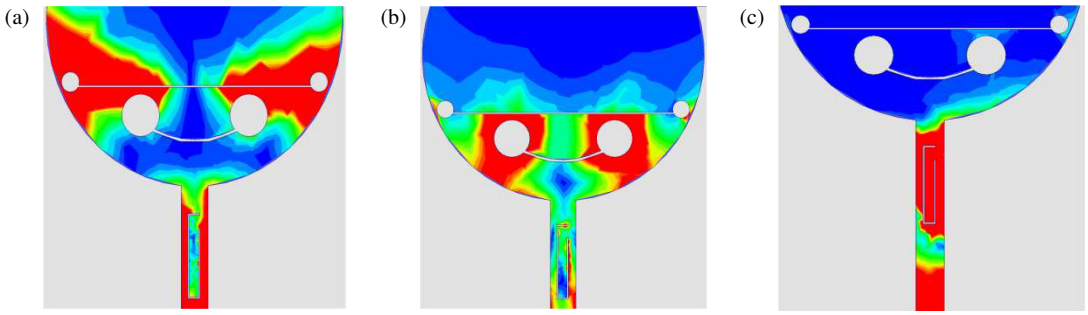

FIGURE 12. Current distribution diagram (a) 3.4 GHz; (b) 4.2 GHz; (c) 7.9 GHz.

centrations occur at the following locations: CRS (3.4 GHz), CRS (4.2 GHz), and the L-shaped slot on the feeder (7.9 GHz). These observations confirm the effective responsiveness of the three target frequency bands within the UWB spectrum to their respective slot structures and the resultant radiation suppression, thereby validating the functionality and reliability of the designed notching structures.

3.3. Envelope Correlation Coefficient and Diversity Gain

Envelope correlation coefficient (ECC) is a critical performance metric used to measure the degree of correlation between wireless communication channels. In MIMO systems, ECC is widely used to quantify the statistical independence of channels between antenna elements. The lower the ECC value is, the weaker the correlation is between antennas. When ECC approaches 0, it indicates that there is almost no correlation between antennas, meaning that the system exhibits high signal independence and excellent diversity gain. In this case, the signals received or transmitted by each antenna are statistically independent in their characteristics, with their signal fades also being uncorrelated. It enables the MIMO technology to fully exploit its advantages, effectively enhancing the system's communication capacity and transmission reliability while minimizing interference and bit error rate. ECC can be calculated using the following formula based on S-parameters:

$$\mathrm{ECC} = \frac{\left|S_{ii} * S_{ij} + S_{ji} * S_{jj}\right|^2}{\left(1 - \left|S_{ii}\right|^2 - S_{ij}^2\right)\left(1 - \left|S_{ji}\right|^2 - S_{jj}^2\right)} \tag{5}$$

Diversity gain (DG) is used to characterize the diversity order of spatial channels. It enables the receiver to achieve a more stable signal-to-noise ratio (SNR), thereby making signal reception more reliable. It should be emphasized that the presence of multipath effects serves as a prerequisite for the realization of DG. Once deprived of the assistance of multipath effects, diversity gain cannot exhibit its unique advantages. Therefore, diversity gain is not only the evidence of improved signal stability but also a full demonstration of the MIMO system's capability to effectively suppress multipath effects.

We can calculate the DG using ECC, and the following equation expresses the relationship between the two.

$$\mathrm{DG} = 10\sqrt{1 - \mathrm{ECC}^2} \tag{6}$$

As shown in Fig. 13, across the antenna's operating frequency band, ECC values remain consistently below 0.0045, while the DG of the antenna exceeds 9.9990 dB throughout the same band, fully meeting the design requirements. Combined with the simulation results, it can be seen that the proposed antenna elements exhibit very low correlation and excellent diversity performance, ensuring that the antennas do not interfere with each other during operation and achieve higher transmission efficiency, making them suitable for high-performance MIMO communication systems.

3.4. Total Active Reflection Coefficient and Channel Capacity Loss

For MIMO antenna systems, since S-parameters cannot fully predict real-world scenarios, it is necessary to calculate the to-

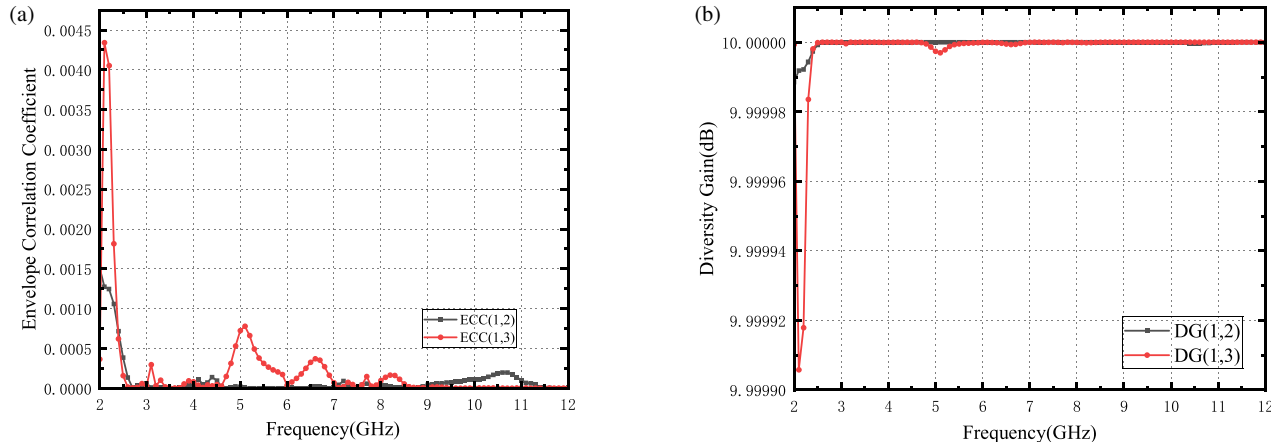

FIGURE 13. (a) ECC; (b) DG.

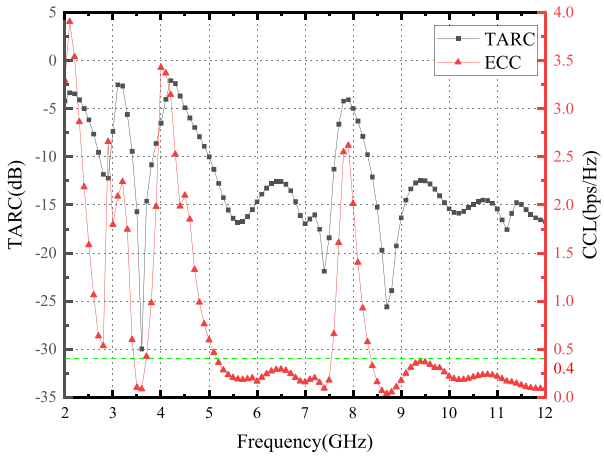

FIGURE 14. TARC and CCL.

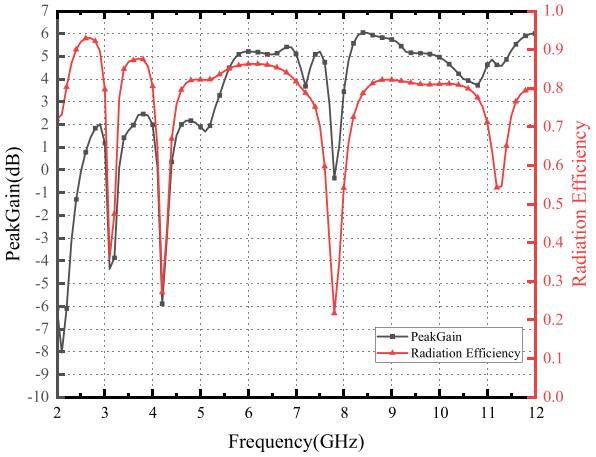

FIGURE 15. Antenna peak gain and radiation efficiency.

tal active reflection coefficient (TARC) of the antenna. TARC can be computed using the following formula based on S-parameters:

$$\mathrm{TARC} = \frac{\sqrt{\sum_{i=1}^{4}\left|S_{i1}+\sum_{n=2}^{4}S_{in}e^{j\theta n-1}\right|^2}}{2} \tag{7}$$

Channel capacity loss (CCL) is also a critical parameter in MIMO antennas. Generally, a CCL value below 0.4 bps/Hz meets the design requirements for MIMO antennas. CCL is expressed as

$$\mathrm{CCL} = -\log_2 \det\left|\psi^R\right| \tag{8}$$

$$\psi^R = \begin{pmatrix} \rho_{11} & \cdots & \rho_{1n} \\ \vdots & \ddots & \vdots \\ \rho_{m1} & \cdots & \rho_{mn} \end{pmatrix} \tag{9}$$

The calculation results, as shown in Fig. 14, indicate that for the UWB-MIMO antenna, except in the notched frequency bands, the TRAC is less than -10 dB and CCL below 0.4 bps/Hz. This further demonstrates that the antenna exhibits very low coupling, ensuring channel independence during signal reception and transmission without mutual interference, thereby enhancing the system capacity.

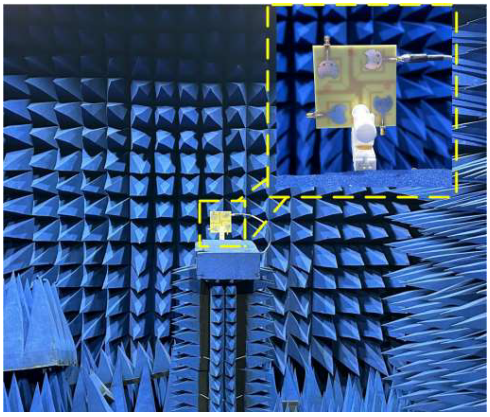

FIGURE 16. Measured results in microwave anechoic chamber.

3.5. Radiation Performance Analysis of the Antenna

Figure 15 shows the peak radiation gain and radiation efficiency of the 4-port MIMO antenna. The gain ranges from 1 to 6.05 dB

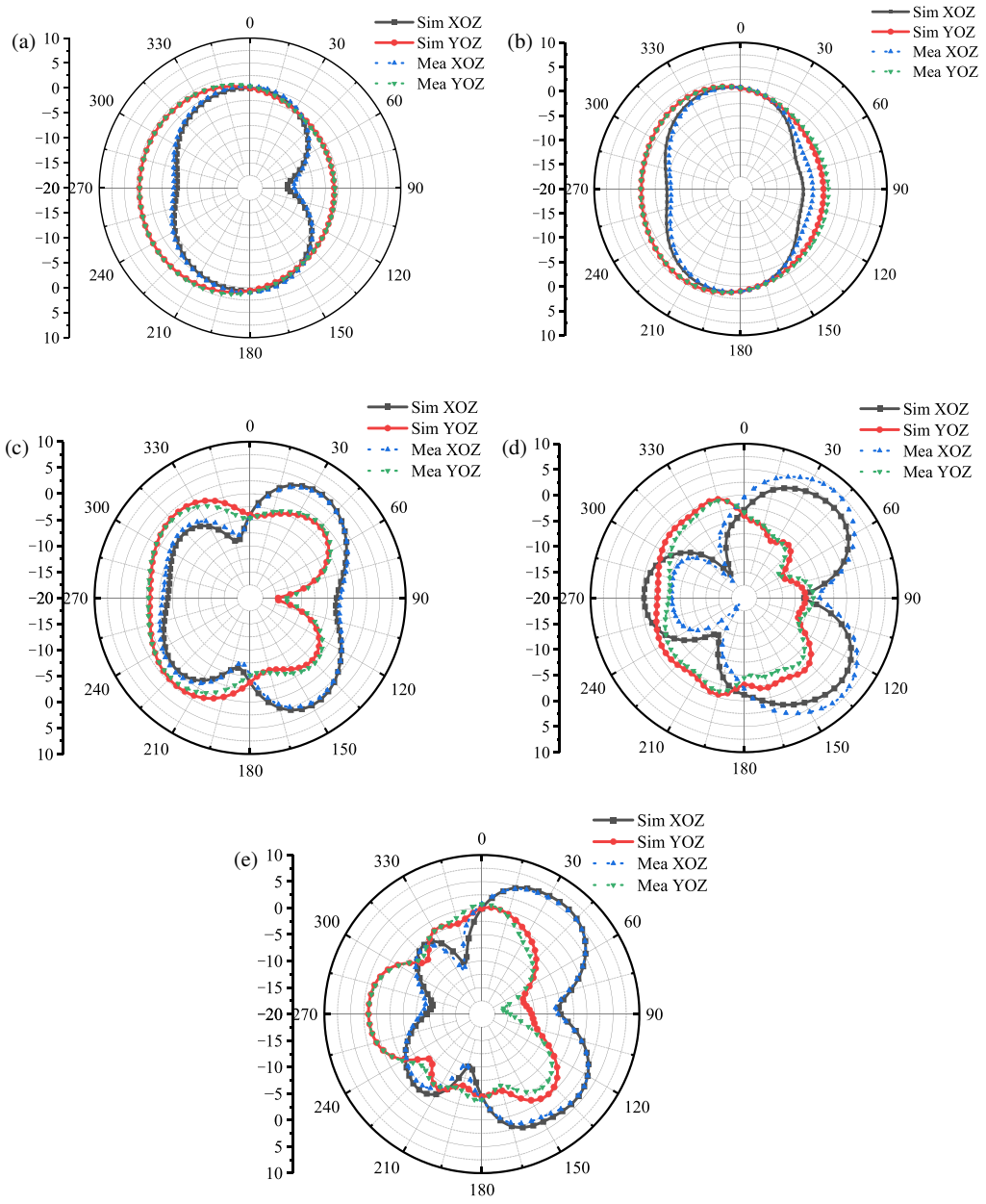

FIGURE 17. 2D radiation patterns (a) 2.9 GHz; (b) 3.6 GHz; (c) 5.6 GHz; (d) 7.8 GHz; (e) 8.7 GHz.

(excluding the notched portion), and the radiation efficiency ranges from 70% to 92%. The gains at the center positions of the notches are -4.35 dB, -5.89 dB, and -0.34 dB, respectively, with radiation efficiencies of 36%, 27%, and 21%. This indicates that signals within this frequency range can be effectively suppressed, further demonstrating the stability of signal suppression in the notched frequency bands.

Figure 16 shows the radiation patterns of the UWB-MIMO antenna in the YOZ and XOZ planes measured in a microwave anechoic chamber.

As can be seen from Fig. 17, in the low-frequency bands (2.9 GHz, 3.6 GHz), the radiation characteristics of the XOZ plane and YOZ plane are relatively similar, both showing no obvious directional radiation capability and relatively uniform overall radiation. As the frequency increases, due to the presence of inverted L-shaped stubs and CSDS, the radiation characteristics change, and a directional radiation trend gradually emerges. At 8.7 GHz, the difference in radiation characteristics between the E-plane and H-plane reaches its maximum: the XOZ plane exhibits strong directional radiation capability, while the YOZ plane has weak radiation at certain angles. This difference enables the antenna to adapt to application scenarios with different directional and radiation intensity requirements at different frequencies, providing a reference for antenna selection and layout in practical applications.

Furthermore, the antenna performance proposed in this paper is evaluated by juxtaposing it with the findings of previous research, and the results are presented in Table 3. A thorough comparison of the performance of each antenna shown in the table has been carried out. It is found that this antenna not only

TABLE 3. Comparison of the proposed antenna with several existing antennas.

Ref.	Size (mm^2)	BW	No. of notches	No. of Ports	Isolation (dB)	ECC
[13]	60×41	3.1–10.6	0	4	< -20	< 0.1
[15]	41×41	3.1–10.8	2	4	< -15	< 0.2
[17]	22×36	3.1–11	1	2	< -15	< 0.1
[18]	38.5×38.5	3.08–11.8	1	2	< -15	< 0.1
[19]	44×44	2.95–10.8	1	4	< -15.5	< 0.08
[20]	39×39	2.3–13.75	2	4	< -22	< 0.02
[21]	34×34	2.5–12	3	4	< -15	< 0.05
[24]	26×26	2.9–11.6	2	2	< -16	< 0.02
[25]	44×48	3–12	3	4	< -20	< 0.16
[26]	35×35	2.96–11.25	2	4	< -17	< 0.012
Proposed	$\mathbf{90 \times 90}$	**2.87–12**	**3**	**4**	$\mathbf{< 24.3}$	$\mathbf{< 0.0045}$

maintains a high level of isolation but also exhibits superior ECC and features three notch frequency bands. It is also worth noting that while ensuring the aforementioned excellent performance, the antenna's overall size of $90 \times 90\,mm^2$ involves a trade-off in terms of miniaturization for portable application scenarios. This size may restrict its integration into compact devices such as wearable electronics or small-sized wireless terminals. The current dimension is a result of balancing multiple performance indicators; arbitrarily reducing the size could lead to performance degradation, such as narrowed operating bandwidth, weakened isolation between ports, or distorted notch characteristics. However, to enhance practical applicability in portable applications, future work can explore strategies to mitigate this trade-off, such as optimizing the layout of the decoupling structure to reduce redundant space, adopting multi-layer substrates for vertical component integration, or exploring new materials with higher dielectric constants to shrink the physical size while maintaining electrical performance. These efforts will further bridge the gap between the antenna's excellent performance and its adaptability to portable scenarios.

4. CONCLUSION

This paper designs and verifies a four-port UWB MIMO antenna with high isolation and three notched-band characteristics. By integrating a CSDS and an improved L-shaped ground plane design, the antenna achieves port isolation $>$ 25 dB, ECC < 0.0045, and DG > 9.9990 dB within the operating frequency band of 2.7–12 GHz. This design significantly reduces the coupling effect between multiple antennas, providing excellent channel independence for high-density MIMO systems and meeting high-reliability requirements for signal parallel transmission in complex electromagnetic environments. The introduction of CRS on the radiating patch and L-shaped slots on the feed line successfully suppresses interferences from WiMAX (3.19 GHz), C-band satellite communications (4.45 GHz), and X-band radar (7.95 GHz). This design addresses the anti-jamming challenges of traditional UWB antennas in multi-band coexisting scenarios and expands their application scope. The antenna's operating bandwidth covers 2.7–12 GHz, compatible with existing UWB standards (3.1–10.6 GHz) and extending to the X-band (below 12 GHz), providing hardware support for future high-frequency communications (such as 6G millimeter waves). Meanwhile, the design based on a low-cost FR4 substrate (dielectric constant 4.4) balances performance and mass-production economy, making it suitable for industrial-scale deployment.

ACKNOWLEDGEMENT

This work was supported in part by the Natural Science Research Project of Anhui Educational Committee under No. 2022AH051583 and in part by the Graduate Innovation Fund of Anhui University of Science and Technology under grant No. 2025cx2077.

REFERENCES

[1] Nie, L. Y., X. Q. Lin, Z. Q. Yang, J. Zhang, and B. Wang, "Structure-shared planar UWB MIMO antenna with high isolation for mobile platform," *IEEE Transactions on Antennas and Propagation*, Vol. 67, No. 4, 2735–2738, 2019.

[2] Ren, J., W. Hu, Y. Yin, and R. Fan, "Compact printed MIMO antenna for UWB applications," *IEEE Antennas and Wireless Propagation Letters*, Vol. 13, 1517–1520, 2014.

[3] Gómez-Villanueva, R. and H. Jardón-Aguilar, "Compact UWB uniplanar four-port MIMO antenna array with rejecting band," *IEEE Antennas and Wireless Propagation Letters*, Vol. 18, No. 12, 2543–2547, 2019.

[4] Li, R. L., Z. Q. Chen, F. Jiang, L. H. Ye, and J.-F. Li, "Three-port ultrawideband MIMO slot antenna with high isolation," *IEEE Antennas and Wireless Propagation Letters*, Vol. 23, No. 12, 4388–4392, 2024.

[5] Rajagopalan, A., G. Gupta, A. S. Konanur, B. Hughes, and G. Lazzi, "Increasing channel capacity of an ultrawideband MIMO system using vector antennas," *IEEE Transactions on Antennas and Propagation*, Vol. 55, No. 10, 2880–2887, 2007.

[6] Labade, R., A. Poddar, J. Y. Siddiqui, S. R. Jondhale, and G. S. Mani, "Design of flower shaped CSRR UWB antenna with integrated Bluetooth and Wi-Max band-notched characteristics," in *2024 IEEE Conference on Antenna Measurements and Applications (CAMA)*, 1–4, Da Nang, Vietnam, 2024.

[7] Lee, J.-M., K.-B. Kim, H.-K. Ryu, and J.-M. Woo, "A compact ultrawideband MIMO antenna with WLAN band-rejected operation for mobile devices," *IEEE Antennas and Wireless Propagation Letters*, Vol. 11, 990–993, 2012.

[8] Tao, J. and Q. Feng, "Compact ultrawideband MIMO antenna with half-slot structure," *IEEE Antennas and Wireless Propagation Letters*, Vol. 16, 792–795, 2017.

[9] Jayant, S. and G. Srivastava, "Close-packed quad-element triple-band-notched UWB MIMO antenna with upgrading capability," *IEEE Transactions on Antennas and Propagation*, Vol. 71, No. 1, 353–360, 2023.

[10] Deng, J.-Y., L.-X. Guo, and X.-L. Liu, "An ultrawideband MIMO antenna with a high isolation," *IEEE Antennas and Wireless Propagation Letters*, Vol. 15, 182–185, 2016.

[11] Bilal, M., R. Saleem, H. H. Abbasi, M. F. Shafique, and A. K. Brown, "An FSS-based nonplanar quad-element UWB-MIMO antenna system," *IEEE Antennas and Wireless Propagation Letters*, Vol. 16, 987–990, 2017.

[12] Li, H. and N. Gong, "An SRR and CSRR based UWB-MIMO antenna," in *2020 IEEE International Symposium on Antennas and Propagation and North American Radio Science Meeting*, 679–680, Montreal, QC, Canada, 2020.

[13] Liu, X.-L., Z.-D. Wang, Y.-Z. Yin, J. Ren, and J.-J. Wu, "A compact ultrawideband MIMO antenna using QSCA for high isolation," *IEEE Antennas and Wireless Propagation Letters*, Vol. 13, 1497–1500, 2014.

[14] Gao, P., S. He, X. Wei, Z. Xu, N. Wang, and Y. Zheng, "Compact printed UWB diversity slot antenna with 5.5-GHz band-notched characteristics," *IEEE Antennas and Wireless Propagation Letters*, Vol. 13, 376–379, 2014.

[15] Wang, X. and Y. Sun, "Ultra-wideband MIMO antenna with double notched band," in *2020 Cross Strait Radio Science & Wireless Technology Conference (CSRSWTC)*, 1–3, Fuzhou, China, 2020.

[16] Li, J.-F., Q.-X. Chu, Z.-H. Li, and X.-X. Xia, "Compact dual band-notched UWB MIMO antenna with high isolation," *IEEE Transactions on Antennas and Propagation*, Vol. 61, No. 9, 4759–4766, 2013.

[17] Liu, L., S. W. Cheung, and T. I. Yuk, "Compact MIMO antenna for portable UWB applications with band-notched characteristic," *IEEE Transactions on Antennas and Propagation*, Vol. 63, No. 5, 1917–1924, 2015.

[18] Kang, L., H. Li, X. Wang, and X. Shi, "Compact offset microstrip-fed MIMO antenna for band-notched UWB applications," *IEEE Antennas and Wireless Propagation Letters*, Vol. 14, 1754–1757, 2015.

[19] Liu, Y.-Y. and Z.-H. Tu, "Compact differential band-notched stepped-slot UWB-MIMO antenna with common-mode suppression," *IEEE Antennas and Wireless Propagation Letters*, Vol. 16, 593–596, 2016.

[20] Tang, Z., X. Wu, J. Zhan, S. Hu, Z. Xi, and Y. Liu, "Compact UWB-MIMO antenna with high isolation and triple band-notched characteristics," *IEEE Access*, Vol. 7, 19 856–19 865, 2019.

[21] Chen, Z., W. Zhou, and J. Hong, "A miniaturized MIMO antenna with triple band-notched characteristics for UWB applications," *IEEE Access*, Vol. 9, 63 646–63 655, 2021.

[22] Zhao, L., Y. Wang, C. Liu, D. Song, C. Hu, C. Li, H. Zhao, and Z. Wang, "Compact circular-shaped MIMO antenna covers UWB bandwidth with four frequently-used band-notched characteristics for multi-scenario applications," *IEEE Access*, Vol. 12, 32 762–32 771, 2024.

[23] Rekha, V. S. D., P. Pardhasaradhi, B. T. P. Madhav, and Y. U. Devi, "Dual band notched orthogonal 4-element MIMO antenna with isolation for UWB applications," *IEEE Access*, Vol. 8, 145 871–145 880, 2020.

[24] Li, Z., C. Yin, and X. Zhu, "Compact UWB MIMO Vivaldi antenna with dual band-notched characteristics," *IEEE Access*, Vol. 7, 38 696–38 701, 2019.

[25] Sushma, T., R. Gogineni, N. V. Ratnam, S. R. Babu, S. Mandava, and P. V. K. Kanth, "A miniaturized quad port highly isolated triple band notched UWB-MIMO diversity antenna," *Progress In Electromagnetics Research C*, Vol. 152, 43–53, 2025.

[26] Lu, X., S. Linghu, F. Peng, and T. Zhang, "A miniaturized ultra-wideband MIMO antenna design with dual-band notched characteristics," *Progress In Electromagnetics Research M*, Vol. 115, 45–58, 2023.